




## Alignment of a flexible platelike particle in shear flow: Effect of surface slip and edges

Catherine Kamal <sup>1</sup>, Simon Gravelle <sup>1</sup> and Lorenzo Botto <sup>2</sup>

<sup>1</sup>*School of Engineering and Material Science, Queen Mary University of London,  
London E1 4NS, United Kingdom*

<sup>2</sup>*Process and Energy Department, 3ME Faculty of Mechanical, Maritime and Materials Engineering,  
TU Delft, 2628 CD Delft, The Netherlands*



(Received 24 February 2021; accepted 8 July 2021; published 18 August 2021)

Rigid platelike particles displaying interfacial slip can attain a constant orientation in a shear flow when the slip length is sufficiently large. But actual thin particles such as single-layer graphene are flexible and prone to bending deformations when exposed to shear stress. To study the effect of bending deformation on the dynamics of flexible platelike particles with large interfacial slip in a shear flow, we develop a two-dimensional (2D) fluid-structure interaction model. Our model is based on coupling the Euler-Bernoulli beam equation with a boundary integral method to solve the hydrodynamic stress at the particle surface. Emphasis is placed on resolving accurately the stress distribution at the edges of the particle. We find that (i) a stable alignment occurs even for relatively flexible particles and that (ii) edges effects on the shape of the plate are important for values of the length-to-thickness aspect ratio as large as 100. Our results are particularly relevant in view of recent research on the hydrodynamics of suspended flexible sheets made of 2D nanomaterials.

DOI: [10.1103/PhysRevFluids.6.084102](https://doi.org/10.1103/PhysRevFluids.6.084102)

### I. INTRODUCTION

Recent developments in the study of colloidal dispersions of atomically thin sheets made of two-dimensional (2D) nanomaterials (e.g., graphene and graphene oxide [1,2], boron nitride [3], molybdenum disulfide [4]) are generating interest into the flow dynamics of deformable thin colloidal particles. When exposed to sufficiently large shear stresses, such platelike particles are prone to bending deformations [5]. The bending energy of single-layer graphene is in the range of  $40\text{--}80kT$  [6,7], where  $kT$  is the thermal energy. This range is similar to those characterizing lipid bilayers [8,9]. Graphene oxide has an even smaller bending energy of the order  $kT$  [10]. Besides their proneness to bending, platelike particles may exhibit slip lengths that are large in comparison to the particles thickness [11,12]. At large Péclet numbers, interfacial slip can suppress the periodic rotation of a rigid platelike colloid suspended in a linear shear flow field, leading to the particle being aligned indefinitely at a small angle with respect to the flow direction [12]. Jeffery's theory, developed for no-slip particles, instead predicts periodic rotations and alignment only in a time-average sense [13]. Therefore, a better understanding of the combined effects of slip and bending deformations in the microhydrodynamics of platelike particles is needed.

While there is a rich theoretical literature on the rotational dynamics of *rigid* platelike colloidal particles in linear shear flow [14–16], current investigations on the dynamics of flexible sheets (e.g., Refs. [17,18]) rest on a computational framework initially developed for slender flexible particles such as fibers [19] and ribbons [20]. This framework, which is inspired by the slender-body approximation [21,22], relies on the assumption that the sheet can be represented as a planar distribution

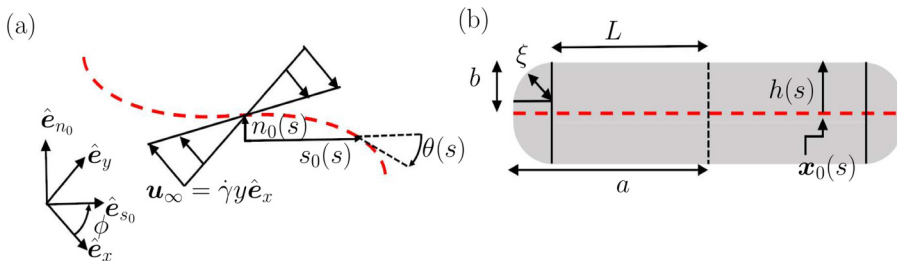


FIG. 1. (a) Sketch of the central line  $\mathbf{x}_0$  (red dashed line) of a flexible 2D platelet in a shear flow field  $\dot{\gamma}y$ . The rotational angle  $\phi$  is measured in the anticlockwise direction from  $\hat{e}_x$ , and  $\theta(s)$  in the clockwise direction from  $\hat{e}_{s_0}$ . (b) Undeformed surface of the 2D platelet. The parameter  $\xi$  is the radius of curvature of the corners.

of regularized stokeslets [23]. Each stokeslet is associated with a restoring elastic force calculated from the bending energy of the sheet. Alternative methods rely on a similar approximation whereby the sheet is instead assumed to be made of a planar distribution of beads and rods [24,25]. In all of these study, hydrodynamic slip has not been considered, and the effects of the ends of the particles are usually neglected. However, the study of the flow dynamics of rigid platelets with slip reveals the importance of accounting for the edges. The aforementioned slip-induced steady alignment of the particle near the flow direction is a consequence of a delicate balance between the hydrodynamic stress over the flat surfaces of the particle and the stress at the edges [12]. Therefore, it is essential to develop a model for flexible platelike particles with slip that include the effects of the edges.

In this paper, we use a two-dimensional model to investigate the effect of deformability on the dynamics of a platelike particle with a large hydrodynamic slip length as compared to the particles half-thickness. The hydrodynamic stress at the particle surface is computed with a boundary integral method (BIM) for Stokes flow, accurately resolving the large stress that form at the edges. The shape of the elastic body suspended in a shear flow is calculated via an iterative method that couples the Euler-Bernoulli beam equation for the deformation of the centerline of the particle with the hydrodynamic load computed using BIM. Similar approaches have been used to find the shapes of flexible rods, either adhered to a wall [26,27] or flowing through a narrow channel [28]. A significant feature of our model is that the body is considered deformable everywhere except at the edges: the edges are treated as rigid elements that provide force and torque boundary conditions for the Euler-Bernoulli beam equation. In addition, our model accounts for the rigid body rotation, enabling a detailed comparison between rigid and flexible platelets in terms of alignment and surface stress distribution.

Since we are motivated by understanding the flow dynamics of 2D nanomaterials, we employ bending rigidity and shear stress values typical of graphene suspensions, as well as aspect ratios as large as allowed by the computational constraints. Besides 2D nanomaterials, the results should also be applicable to clays [29], two-dimensional polymers [30], and extended aromatic molecules [31,32].

## II. FORMULATION

### A. Description of the problem

We consider an inextensible platelike particle suspended in a linear shear flow field  $\mathbf{u}_\infty = \dot{\gamma}y\hat{e}_x$ . For the simulation, we adopt a two-dimensional model: The platelet has infinite extent in the direction of the vorticity ( $\hat{e}_z$ ) with a normal in the flow-gradient plane ( $\hat{e}_x, \hat{e}_y$ ). Deformations and rotations of the platelet are thus restricted to the ( $\hat{e}_x, \hat{e}_y$ ) plane [Fig. 1(a)]. For three-dimensional platelets, such as disks, deformations in the  $\hat{e}_z$  direction are possible. However, calculations of the traction over a clamped axisymmetric disk with the no-slip boundary condition reveals that the traction in the  $\hat{e}_z$  direction is subdominant to the traction in the flow-gradient plane [15]. Therefore,

our two-dimensional approximation is expected to hold for any platelike particle oriented with its longitudinal axis in the direction of the shear.

The undeformed platelet is assumed to be symmetric about the two orthogonal lines passing through its center. In addition, the center of the platelet is initially at the origin of the coordinate system, so the platelet rotates without translating. Because of the symmetries of the undeformed configuration, deformations are symmetric with respect to the line  $y = 0$  at all times. The platelet has length  $2a$  and maximum thickness  $2b$ .

While our fluid-structure interaction method can be applied to any slender surface, we use a surface (line in 2D) that provides the best fit, from a hydrodynamic point of view, to molecular dynamics simulations of graphene platelets in Newtonian fluids [12,33] [Fig. 1(b)]. Graphene platelets are layered material made from stacks of carbon layers. For a single layer graphene platelet, the surface is approximately a rectangle with half-thickness  $b = \xi$  and with semicircle edges of radius  $\xi$ . Here  $\xi$  corresponds to the effective radius of the carbon atoms; for graphene in water,  $\xi \approx 1.8\text{--}2.5 \text{ \AA}$  [32,34]. For multilayer graphene,  $b(n) = (n - 1)d_{\text{gg}}/2 + \xi$ , where  $d_{\text{gg}} \approx 3.35 \text{ \AA}$  [35] is the interlayer distance and  $n$  to the number of layers. For  $n = 1$ ,  $b \approx 0.25 \text{ nm}$  and for  $n = 10$ ,  $b \approx 1.8 \text{ nm}$ . For  $n > 1$ , each edge region consists of a flat face perpendicular to the centerline of half-length  $b - \xi$ , as well as two rounded corners of radius  $\xi$ . The edges are more blunt the larger  $n$ . In general, the bending rigidity of the particle  $\sigma_b$  will depend on  $n$ . For a homogeneous plate, the bending rigidity  $\sigma_b \propto b^3$  [36]. For a multilayer graphene platelet, this relationship appears to work well for multilayer graphene with  $n \leq 10$  [37]. For single layer graphene  $\sigma_b \approx 1\text{--}2 \text{ eV}$  [6,7], and for bilayer graphene  $\sigma_b \approx 36 \text{ eV}$  [38].

The platelet surface is parametrized as  $S = (s_0(s) \pm h(s) \sin \theta(s), n_0(s) \pm h(s) \cos \theta(s)) : -a \leq s \leq a$ . Here  $\mathbf{x}_0(s) = (s_0(s), n_0(s))$  is the centerline of the platelet,  $h(s)$  is the half-thickness of the platelet (in the direction normal to the centerline) and  $\theta(s)$  is the clockwise angle from  $\hat{\mathbf{e}}_{s_0}$  to the tangent of the centerline  $\mathbf{x}_0(s)$  as shown in Fig. 1. The frame  $(\hat{\mathbf{e}}_{s_0}, \hat{\mathbf{e}}_{n_0})$  is the frame of reference attached to the center of the particle. Since the centerline is inextensible, it can be expressed in curvilinear coordinates as:

$$n'_0 = -\sin \theta, \quad s'_0 = \cos \theta, \quad \theta' = \kappa, \quad (1)$$

where the prime denotes the derivative with respect to  $s$ . In the laboratory frame  $(\hat{\mathbf{e}}_x, \hat{\mathbf{e}}_y)$ , the tangent to  $\hat{\mathbf{e}}_{s_0}$  is inclined by an angle  $\phi$  with respect to  $\hat{\mathbf{e}}_x$ . For rotation of the platelet in the direction of the undisturbed vorticity associated to the external flow field,  $\phi < 0$ . Because the curvilinear coordinate system is fixed with respect to the particle, we have  $\theta(0) = 0$ .

For the specific surface considered here,  $h(s)$  is symmetric about  $s = 0$ . Under this parametrization, the surface  $S$  is split in two regions (Fig. 1): a ‘‘slender’’ region  $\{h(s) = b/a : -L \leq s \leq L\}$  for  $L = a - \xi$ , and an ‘‘edge’’ region of length  $\xi$  for  $L < |s| \leq a$ .

The difference between the present formulation and the one of Refs. [12,33] is that the slender region is now free to deform due to the applied external hydrodynamic force and torque. The slender region of the platelet deforms to leading order like a flexible beam with bending rigidity  $\sigma_b$ . At the edge regions, however, the slender approximation no longer holds. It is thus assumed that the edges are rigid, as done in Refs. [26,27].

## B. Governing equations and fluid-structure interaction

The platelet is freely suspended in a fluid of viscosity  $\eta$ . The flow field  $\mathbf{u}$ , the pressure field  $p$ , and the stress tensor  $\boldsymbol{\sigma}$  are assumed to satisfy the Stokes equations:

$$\nabla \cdot \boldsymbol{\sigma} = 0, \quad \sigma_{ij} = -\delta_{ij}p + \eta \left( \frac{\partial u_i}{\partial x_j} + \frac{\partial u_j}{\partial x_i} \right). \quad (2)$$

On the platelet surface  $S$ , we prescribe a Navier slip boundary condition

$$\mathbf{u}_{\text{sl}} = \frac{\lambda}{\eta} \mathbf{n} \times \mathbf{f} \times \mathbf{n}, \quad (3)$$

where  $\mathbf{f} = \boldsymbol{\sigma} \cdot \mathbf{n}$  is the hydrodynamic traction,  $\mathbf{n}$  is the outward-pointing normal to the surface,  $\mathbf{u}_{\text{sl}}$  is the hydrodynamic slip velocity and  $\lambda$  is the slip length [39,40]. The use of a single slip parameter  $\lambda$  for the whole surface  $S$  leads to a distribution of surface traction that compares well with molecular dynamics simulations of single- or multi-layer graphene particles in water [12,32].

Due to the high resolution requirement to resolve the flow around a thin body, particularly in the edge regions, we compute the hydrodynamic load by using the BIM for Stokes flow [41]. The boundary integral formulation gives the following relation between  $\mathbf{f}$ ,  $\mathbf{u}_{\text{sl}}$  and the velocity of the platelet  $\mathbf{u}_D$  at each point  $\mathbf{x}_1$  on the surface  $S$ :

$$\int_S \mathbf{n} \cdot \mathbf{K}(\mathbf{x} - \mathbf{x}_1) \cdot \mathbf{u}_{\text{sl}} dS(\mathbf{x}) - \frac{1}{\eta} \int_S \mathbf{G}(\mathbf{x} - \mathbf{x}_1) \cdot \mathbf{f} dS(\mathbf{x}) = \mathbf{u}_D(\mathbf{x}_1) + \frac{\mathbf{u}_{\text{sl}}(\mathbf{x}_1)}{2} - \mathbf{u}_\infty(\mathbf{x}_1). \quad (4)$$

The second-order tensor  $\mathbf{G}$  and the third-order tensor  $\mathbf{K}$  are respectively [41]:

$$G_{ij}(s, h) = \frac{1}{4\pi} \left( -\delta_{ij} \ln r + \frac{x_i x_j}{r^2} \right), \quad K_{ijk}(s, h) = -\frac{1}{\pi} \frac{x_i x_j x_k}{r^4}, \quad r = \sqrt{s^2 + h^2}.$$

For  $\lambda = 0$ , the term containing the  $K$  tensor vanishes and Eq. (4) reduces to the formulation for a rigid platelet (cf. Ref. [26]). The platelet is free to move with a velocity  $\mathbf{u}_D = \dot{s}_0 \hat{\mathbf{e}}_{s_0} + \dot{n}_0 \hat{\mathbf{e}}_{n_0} + \Omega_D \hat{\mathbf{e}}_z \times (\mathbf{x}_1 - \mathbf{x}_0) + \Omega \hat{\mathbf{e}}_z \times (\mathbf{x}_1 - \mathbf{x}_c) + \dot{\gamma} y_c \hat{\mathbf{e}}_x$ . Here, the first three terms on the right of the equal sign are associated with the time-dependent deformations of the platelet, and the final terms are associated with rigid body motion. The term  $\Omega$  is the angular velocity of a torque-and-force free platelet about its center of inertia  $\mathbf{x}_c$  and  $\dot{\gamma} y_c \hat{\mathbf{e}}_x$  is the uniform velocity at which the particles translates. To find  $\Omega$ , we solve Eq. (4) together with the constraint of zero hydrodynamic torque [42]

$$T \equiv \hat{\mathbf{e}}_z \cdot a \int_S (\mathbf{x} - \mathbf{x}_c) \times \mathbf{f} dS = 0. \quad (5)$$

Because  $\mathbf{x}_0$  is in our case antisymmetric about  $s = 0$ ,  $\theta(-s) = \theta(s)$ , then  $\mathbf{x}_c$  is located at the center of the platelet. We set  $\mathbf{x}_c$  to be at the center of our choice of coordinate system.

The effect of the hydrodynamic flow field is to exert a distributed force and a distributed torque over the platelet, which will in turn cause the platelet to rotate and deform. To separate the contributions of the traction that produce a distributed load normal to the surface of the platelet from those producing a couple, we split the traction in its antisymmetric and symmetric parts with respect to the centerline:

$$\begin{aligned} \Delta g_i(s, h) &= \text{Asym}\{f_i(s, h)\} = f_i(s, h) - f_i(s, -h), \\ g_i(s, h) &= \text{Sym}\{f_i(s, h)\} = f_i(s, h) + f_i(s, -h). \end{aligned} \quad (6)$$

With the above notation, the platelet is subject to external normal and tangential force densities, respectively  $g_n(s) = \mathbf{g} \cdot \hat{\mathbf{e}}_n$  and  $g_s(s) = \mathbf{g} \cdot \hat{\mathbf{e}}_s$ , as well as a total torque density

$$\begin{aligned} q(s) &= \hat{\mathbf{e}}_z \cdot \{[\mathbf{x}^+(s) - \mathbf{x}_0(s)] \times \mathbf{f}(s, h) + [\mathbf{x}^-(s) - \mathbf{x}_0(s)] \times \mathbf{f}(s, -h)\} \\ &= h(s)[\Delta g_{n_0}(s) \sin \theta(s) - \Delta g_{s_0}(s) \cos \theta(s)], \end{aligned} \quad (7)$$

acting on the ‘‘slender’’ region of the central line of the platelet. Here  $\mathbf{x}^+$  is the coordinate of the top surface of the platelet, and  $\mathbf{x}^-$  the corresponding coordinate of the bottom surface i.e.,  $\mathbf{x}^\pm = (s_0 \pm h \sin \theta, n_0 \pm h \cos \theta)$ . Because the edges are treated separately from the slender region in our fluid-structure interaction model, we also define a (scalar) edge torque and force respectively:

$$\begin{aligned} T_E(\pm L) &= \hat{\mathbf{e}}_z \cdot \int_{S_E(\pm L)} (\mathbf{x} - \mathbf{x}_0) \times \mathbf{f} dS, \\ \mathbf{F}_E(\pm L) &= \int_{S_E(\pm L)} \mathbf{f} dS, \quad \mathbf{F}_E = F_{E,s} \hat{\mathbf{e}}_s + F_{E,n} \hat{\mathbf{e}}_n, \end{aligned} \quad (8)$$

where  $S_E(-L)$  and  $S_E(L)$  are the surfaces of the edges regions, and edges torques are calculated with respect to the points  $x_0(s = \pm L)$ , respectively. Usually, this edge torque and force are assumed to be zero for slender bodies (see, for example, Ref. [19]). When the particle is almost aligned with the flow, however, the traction on the edge region becomes important: The torque distribution over a particle aligned with the flow results from a delicate balance between the torque produced over the slender region of the particle and from the edges [15]. Equations 8 represent the (scalar) edge torque and force produced from this traction.

The equilibrium equations determining the shape of the centerline are (see Appendix)

$$\sigma_b \theta''' + l \theta' + g_n + q' = 0, \quad l' + g_s = 0, \quad (9)$$

to be solved subject to the boundary conditions

$$\begin{aligned} \sigma_b \theta'(-L) &= T_E(-L), \\ \sigma_b \theta''(-L) &= -q(-L) + F_{E,n}(-L), \\ \theta(s) &= \theta(-s), \\ \theta(0) &= 0, \\ l(-L) &= F_{E,s}(-L). \end{aligned} \quad (10)$$

Here  $l$  is the axial tension. Equations (9) represent force balances on the central line, in the normal and tangential directions, respectively. The equation on the top represents a balance between the normal elastic restoring forces due to bending  $\sigma_b \theta'''$  and tension  $l$ , and the forces due to the fluid. Equations (9) is identical, for example, as that used in Ref. [43], with the exception that we include hydrodynamic torque density, edge forces, and edge torques. Equations (9) will be solved together with Eqs. (10) to find the equilibrium shape of the flexible platelet with slip in shear flow.

Making length, time, and stress nondimensional by using  $a$ ,  $1/\dot{\gamma}$ , and  $\dot{\gamma}\eta$  respectively, Eqs. (9) become

$$\tilde{\sigma} \theta''' + \tilde{l} \theta' + \tilde{g}_n + \tilde{q}' = 0, \quad \tilde{l}' + \tilde{g}_s = 0. \quad (11)$$

Here and in the following, dimensionless units are denoted with a tilde. The dimensionless equations for the deflection of the platelet [Eqs. (11)] depend on the dimensionless rigidity parameter  $\tilde{\sigma} = \sigma_B / \dot{\gamma} \eta a^3$ . For a homogeneous material,  $\sigma_B$  scales as  $\sigma_B \sim B b^3$  [37,46], and for graphene  $B = [2.3-7] \times 10^{11} \text{ N m}^{-2}$  [38]. Therefore, the dimensionless parameter can be expressed in terms of the length to thickness aspect ratio

$$\tilde{\sigma} = B \left( \frac{b}{a} \right)^3 \frac{1}{\dot{\gamma} \eta}. \quad (12)$$

Note that this parameter is different from the corresponding parameter for rods,  $B(b/a)^4 / (\dot{\gamma} \eta)$  [19], because of the different scaling of the second moment of cross-sectional area with  $b$ .

A color map of the rigidity parameter  $\tilde{\sigma}$  in the aspect ratio ( $a/b$ )–shear stress ( $\dot{\gamma} \eta$ ) space is shown in Fig. 2, with some typical values related to graphene. The black line marks  $\tilde{\sigma} = 1$ , the order of magnitude estimate compatible with the result for the buckling of no-slip plates as predicted from the model of Ref. [5]. For a given value of  $\dot{\gamma} \eta$ ,  $\tilde{\sigma}$  varies by orders of magnitude due the inverse cubic dependence with respect to the geometric aspect ratio. The aspect ratio of typical layered materials such as graphene and clay platelets can vary dramatically (cf. Ref. [47]). Thus, depending on the actual aspect ratio of the platelet, a graphene platelet in a typical large shear stress  $\dot{\gamma} \eta = 2 \times 10^4 \text{ Pa}$  will appear rigid ( $\tilde{\sigma} < 1$ ) if  $a/b \lesssim 300$ , while a platelet with a larger aspect ratio will appear flexible ( $\tilde{\sigma} > 1$ ).

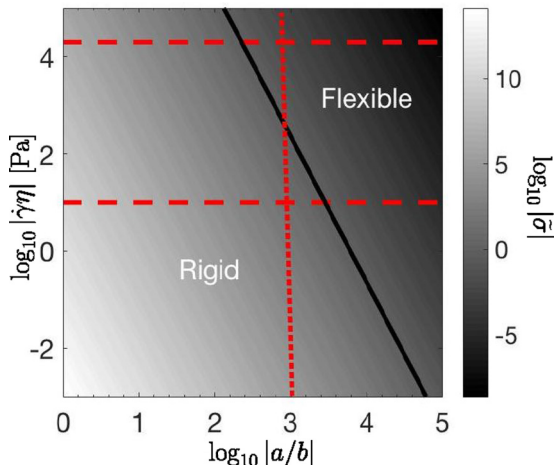


FIG. 2. Map of nondimensional rigidity parameter  $\bar{\sigma}$  vs geometric aspect ratio  $a/b$  and shear stress  $\dot{\gamma}\eta$ . Full black line: Threshold  $\bar{\sigma} = 1$  below which buckling is expected, from Ref. [5]. Vertical dotted red line: Typical aspect ratio of single-layer graphene (assuming half-thickness 0.5 nm and half-length 0.5  $\mu\text{m}$ ). Bottom horizontal dashed red line: Typical shear stress during liquid-phase exfoliation of graphene, from Ref. [44] ( $\dot{\gamma}\eta = 10$  Pa). Top horizontal dashed red line: typical maximum shear stress for mixing of carbon nanoparticles in polymer mixing from Ref. [45] ( $\dot{\gamma}\eta = 2 \times 10^4$  Pa).

### III. NUMERICAL METHOD TO FIND STABLE SOLUTIONS

Rigid platelets attain stable aligned solutions in shear flow if the slip length is greater than some critical slip length  $\lambda_c \sim b$  [12]. In this section we describe a numerical procedure to test if a stable aligned solution also exists for a flexible platelet. We use an iterative method to find such solution to the coupled Eqs. (4), (10), and (11) as  $\bar{\sigma}$  decreases from a value corresponding to a rigid platelet ( $\bar{\sigma} \rightarrow \infty$ ). Stationary solution corresponds to  $\mathbf{u}_D = \mathbf{0}$ . Under this condition, Eq. (4) simplifies to

$$\int_S \mathbf{n} \cdot \mathbf{K}(\mathbf{x} - \mathbf{x}_1) \cdot \mathbf{u}_{\text{sl}} dS(\mathbf{x}) - \frac{1}{\eta} \int_S \mathbf{G}(\mathbf{x} - \mathbf{x}_1) \cdot \mathbf{f} dS(\mathbf{x}) = \Omega \hat{\mathbf{e}}_z \times \mathbf{x}_1 + \frac{\mathbf{u}_{\text{sl}}(\mathbf{x}_1)}{2} - \mathbf{u}_{\infty}(\mathbf{x}_1). \quad (13)$$

In contrast to other models such as that applied in Ref. [28], we have included the rotational angular velocity  $\Omega$  since we need to find the orientation of the platelet  $\phi = \phi_c$  for which  $\Omega(\phi_c) = 0$ . The quasisteady “stationary” solution of the platelet at the  $n^{\text{th}}$  time step  $t^n$  is found by the following iterative procedure:

*Step 1: Time iteration.* Advance the time by an increment  $dt^{(n)}$ ,  $t^n = t^{n-1} + dt^{(n)}$ , and the rotational angle of the platelet according to  $\phi^n = \phi^{n-1} + dt^{(n)}\Omega^{n-1}$ .

*Step 2: Calculation of the traction.* Starting from an initial guess  $\mathbf{x}^n \approx \mathbf{x}^{n,g_1}$  for the configuration of the central line, solve Eq. (13) to find the corresponding hydrodynamic traction  $\mathbf{f}^{n,g_1}$  and rotational velocity  $\Omega^{n,g_1}$  for a platelet oriented at the angle  $\phi^n$  (details are given in Sec. III A).

*Step 3: Calculation of the equilibrium shape.* Using  $\mathbf{f}^{n,g_1}$ , find a new equilibrium shape  $\mathbf{x}^{n,g_2}$  by solving Eq. (11) using a Newton residual method (details are given in Sec. III B).

*Step 4: Convergence of the numerical procedure.* Repeat Step 2 and 3 until convergence. If convergence is achieved, repeat Step 1 to find the inclination angle at the new time  $t^{n+1} = dt^{(n+1)} = dt^{(n)}$ . If no equilibrium shape is found after a maximum number of iterations, reduce the timestep  $dt^{(n)}$  and repeat Step 1.

The existence of a stable solution is determined by monitoring  $\Omega^n$ . If  $\Omega^n \rightarrow 0$  as  $t$  increases, then a stationary solution is found. Otherwise, no stable aligned solution exists and the platelet follows a rotational trajectory similar to that predicted by Jeffery for a rigid particle [13].

The Newton residual method can converge in just a few iterations, provided that the initial guess is close to the actual solution. We achieve such good convergence by first computing the deformed shape for an almost rigid body ( $\tilde{\sigma}[1] = 10$ ), before slowly decreasing  $\tilde{\sigma}$ . Here  $\tilde{\sigma}[i]$  represents the decreasing order values of  $\tilde{\sigma}$  for which a stable aligned solution is found. For the first value,  $\tilde{\sigma} = \tilde{\sigma}[1]$ , we use the stable solution of a rigid undeformed body oriented at  $\phi_c$  as the initial guess, and for the second, and slightly reduced, value  $\tilde{\sigma}[2]$ , we use the final profile from the previous step as the initial guess. For the following steps, the last two profiles for  $\tilde{\sigma}[i - 1]$  and  $\tilde{\sigma}[i - 2]$  are used to approximate an initial guess of the profile for the given  $\tilde{\sigma}[i]$ . The guess is calculated from a two-point extrapolation method for  $i = 2$  and a three-point extrapolation method for all other steps, using polynomial extrapolation [48].

### A. Step 2: Calculation of the traction

To compute  $\mathbf{f}$  for a given platelet shape and orientation from Eq. (13), we use the BIM scheme described in Refs. [12,33]. This method involves discretizing  $\mathbf{f}$  and  $\mathbf{u}_{sl}$  in Eq. (13) as piece-wise constant functions each centered at the midpoint of  $N$  subintervals along the surface. With this discretization, Eq. (13) results in  $2N$  linear equations for the components of  $\mathbf{f}$ , which can be solved given the surface shape and orientation  $\phi$  of the platelet. This numerical solution for  $\mathbf{f}$  is, however, not unique as it is defined up to some function  $p_0\mathbf{n}$ , with  $\mathbf{n}$  the normal to the surface. Such nonuniqueness is generic to incompressible flows: an incompressible velocity field is unique up to a constant ambient pressure  $p_0$ . For a flat body, this prefactor does not affect the load since the term  $p_0\mathbf{n}$  cancels from the load distribution  $g_n + q$  by symmetry. For a deformable body, on the other-hand, this extra prefactor can induce variations in the load distribution. The thin-plate equation for the solid (Euler-Bernoulli beam equation), however, implicitly assumes no deformation in the direction normal to the central line. Hence, we can set  $p_0 = 0$  with no error beyond the small error already accepted by using the Euler-Bernoulli beam theory. To set  $p_0 = 0$ , we use the precondition method described by Pozrikidis [49].

To test the validity of our numerical procedure for the computation of  $\mathbf{f}$ , we compare our results to the analytical solution for a no-slip cylinder [50] and a slip cylinder (Supplementary Information (SI) of Ref. [12]). In both cases we find spatial convergence with error proportional to the square of the grid mesh size (cf. SI of Ref. [12]). We also test our procedure in the limit  $a/b \rightarrow \infty$  by comparing to the analytical solution for the rotational drag coefficient  $F_d$  for no-slip plates of zero thickness ( $F_d \rightarrow 2\pi\eta a^3$ ) [51]. We find that  $F_D$  converges to Sherwood and Meeten's prediction for  $a/b \rightarrow \infty$  for particles of any slip length  $\lambda$  as expected (the torque applied to a plate held fixed in a rotational flow field becomes independent of  $\lambda$  as  $a/b \rightarrow \infty$  [33]).

### B. Step 3: Calculation of the equilibrium shape

As in Step 2, the platelet is fixed at an orientation  $\phi$  with respect to the flow and satisfies Eqs. (11) with the boundary conditions Eqs. (10) for  $\theta$ , as well as the curvilinear Eqs. (1) with the boundary conditions  $s_0(0) = n_0(0) = 0$  for  $\mathbf{x}_0$ . In order to find  $\mathbf{x}_0$ , we first solve Eqs. (11) to find  $\theta$ , and then Eqs. (1) to find  $\mathbf{x}_0$  for a given  $\theta$ . To numerical solve Eqs. (11), the load distribution (LOAD =  $g_n + q'$ ) and  $\theta$  are interpolated onto  $N_f$  evenly spaced grid points  $\{\text{LOAD}(s_1), \dots, \text{LOAD}(s_{N_f}) : s_1 = -L, \dots, s_{N_f} = 0\}$  and  $\{\theta(s_1), \dots, \theta(s_{N_f}) : s_1 = -L, \dots, s_{N_f} = 0\}$  by the interpolation polynomial [52]. The spacing between the points is  $\Delta s = L/(N_f - 1)$ . Equations 11 with the given boundary conditions are then discretized using a second-order finite difference scheme [43], to produce a set of  $2N_f$  linear equations for  $\theta(s_i)$ , with  $i = 1, \dots, N_f$ . The system of equations is solved using the Newton residual method [48]. Once  $\theta(s_i)$  is found to a given tolerance, then the profile shapes are found similarly to  $\theta(s_i)$ : The curvilinear equations are first discretized to produce a set of  $4N_f$  linear equations for  $s_0(s_i)$  and  $n_0(s_i)$ , and this system of equations is then solved by the Newton residual method to find  $\mathbf{x}_0$ .

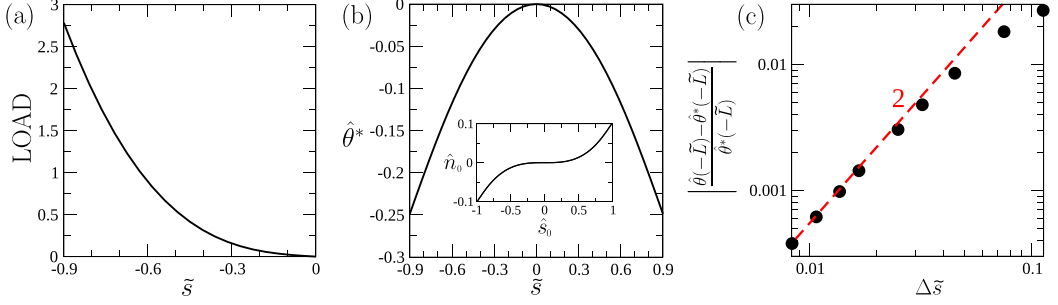


FIG. 3. (a) Polynomial load from Eq. (14) as a function of  $\tilde{s}$ . (b) Analytical solution  $\hat{\theta}^*$  of Eq. (14) as a function of  $\tilde{s}$ . Inset: Corresponding profile of out-of-plane displacement. (c) Error between the analytical solution  $\hat{\theta}^*$  and the numerical solution  $\hat{\theta}$  at  $\tilde{s} = -\tilde{L}$  versus the grid spacing  $\Delta\tilde{s}$ . The parameters of Eq. (14) are  $a_1 = 0.47$ ,  $a_2 = 0.005$ , and  $a_3 = -0.01$ .

To confirm the  $\mathcal{O}(\Delta s^2)$  spatial convergence, we compare our numerical solution to Eq. (11) with an assigned polynomial load

$$\hat{\theta}^{*'''} = c\tilde{s}^3 + a_3\tilde{s}, \quad (14)$$

and  $\hat{\theta}^{*'}(-\tilde{L}) = a_1$ ,  $\hat{\theta}^{*''}(-\tilde{L}) = a_2$ ,  $\hat{\theta}^*(0) = 0$ , and  $\hat{\theta}^*(\tilde{s}) = \hat{\theta}^*(-\tilde{s})$ . Here  $a_1$ ,  $a_2$ , and  $a_3$  are arbitrary parameters and  $c$  is an extra variable ensuring that the boundary condition  $\hat{\theta}^*(0) = 0$  is met. The exact solution for  $\hat{\theta}^*$  for given values of  $a_1$ ,  $a_2$ , and  $a_3$  is shown in Fig. 3(b) along with the load  $\hat{\theta}^{*'''}$  in Fig. 3(a) [the hat symbol is used to represent the solution of Eq. (14)]. A comparison between the analytical and numerical solutions for  $\hat{\theta}^*(-\tilde{L})$ , confirms the  $\mathcal{O}(\Delta\tilde{s}^2)$  spatial convergence [Fig. 3(c)].

### C. Step 4: Convergence of the numerical procedure

To confirm the convergence of the full numerical procedure involving both hydrodynamic force calculation from the BIM method and the Euler-Bernoulli beam equation resolution, we compare a stable solution found for a different number  $N$  of surface grid points. Examples of stable solutions for a rigid and a flexible platelet are shown in Figs. 4(a) and 4(b), respectively. We use the maximum deformation  $\tilde{n}_0(-\tilde{L})$  to compare the stable solution for different number  $N$  of surface grid points. Figure 4(c) confirms the convergence of  $\tilde{n}_0(-\tilde{L})$  as  $N$  is increased. More specifically, for  $a/b = 10$  and  $\tilde{\lambda} = 8$ , we find that a good convergence is obtained for  $N \geq 72$ . For higher aspect ratio, a larger number of grid points is needed to ensure the resolution of the traction at the edges. Unless otherwise stated, in our simulations we use  $N = 120$ .

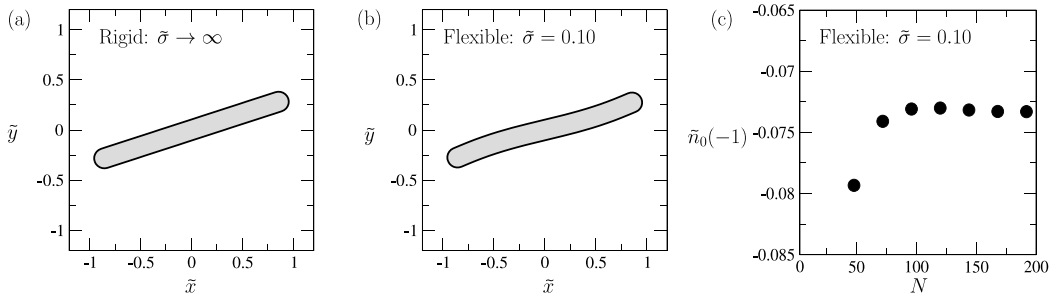


FIG. 4. Stable solution for (a) a rigid platelet and (b) a flexible platelet with  $\tilde{\sigma} = 0.1$ . (c) Convergence of the maximum centerline displacement versus the number of grid points  $N$ . Here  $\tilde{\lambda} = 8$  and  $a/b = 10$ .



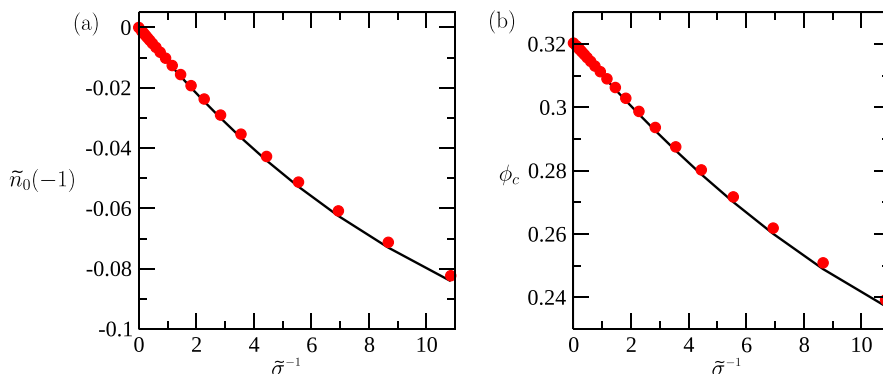


FIG. 5. (a) Maximum deflection  $\tilde{n}_0(-1)$  and (b) orientation angle  $\phi_c$  for the stable solution, comparing the cases in which  $\tilde{l}(\tilde{s})$  is included in Eqs. (11) (red disks) or excluded from it (black lines), respectively. As in Fig. 4,  $\tilde{\lambda} = 8$  and  $a/b = 10$ .

#### IV. ALIGNMENT OF A FLEXIBLE PLATELET WITH SLIP

We adopt the iterative procedure outlined in Sec. III to find stable configurations of a flexible platelet with slip for different values of the rigidity parameter  $\tilde{\sigma}$ . From here forward, we present results in nondimensionlized form (where, we recall, we have used  $a$ ,  $\eta\dot{\gamma}$  and  $1/\dot{\gamma}$  as length, stress and timescales). Our calculations reveal that, as long as the slip length  $\tilde{\lambda}$  is greater than a critical value  $\tilde{\lambda}_c$  and the rigidity parameter  $\tilde{\sigma}$  is greater than  $\tilde{\sigma}_c$ , a stable solution can be found. Our results also show that the value of  $\tilde{\sigma}_c$  depends on  $\tilde{\lambda}$  and on the specific shape of the platelet (i.e., its aspect ratio  $a/b$  and the shape of the ends). For the case considered in Fig. 4, with  $n = 1$ ,  $\tilde{\lambda} = 8$  and  $a/b = 10$ , we find  $\tilde{\sigma}_c \approx 0.09$ .

In what follows, we evaluate the maximum deflection of platelets  $\tilde{n}_0(-1)$  and the equilibrium angle  $\phi_c$  for different values of  $\tilde{\sigma}$ . At constant aspect ratio, a decreasing value of  $\tilde{\sigma}$  corresponds to an increase in the shear stress. Only values  $\tilde{\sigma} \geq \tilde{\sigma}_c$  are considered, as for  $\tilde{\sigma} < \tilde{\sigma}_c$ , our code fails to converge between Step 2 and Step 3 (the sequence of guess solutions  $\{\tilde{\mathbf{x}}^{n, s_i}\}$  does not converge as the number of iterations increases). We use  $n = 1$  unless otherwise stated, and we consider a range of slip lengths spanning from  $\tilde{\lambda} \ll 1$  to  $\tilde{\lambda} \gg 1$ . For typical graphene suspensions,  $\tilde{\lambda} \ll 1$  [53], however, the case  $\tilde{\lambda} \gg 1$  is in principle possible for extremely small graphene flakes or small aromatic molecules [32].

Before analyzing the effects of slip and edges, we start by making some observations. First, the deformation of the platelet at its stable orientation is small in comparison to that expected at the corresponding value of  $\tilde{\sigma}$  from the buckling theory for no-slip disks [5]. For instance, Fig. 4(c) shows that for  $\tilde{\sigma} = 0.1$ , the maximum deflection of the platelet is only  $|\tilde{n}_0(-1)| \approx 0.073$ . One reason for the small deflection is the orientation of the platelet with the flow. For an elongated particle in a shear flow, maximum deformations occur when the long axis of the body is oriented along the compressional axis of the flow, i.e.,  $\phi = \pm\pi/4$ . While this situation is expected for rotating particles such as no-slip rods and platelets [5,54], it is not the case for slip platelets with large values of  $a/b$ , for which  $\phi_c \ll 1$  [12]. For  $\phi = 0$ , the compressive component of the flow ( $\tilde{g}_x$ ) is equal to zero for an undeformed platelet and is small for a slightly deformed platelet. For a platelet oriented near the flow direction, the deflection of the centerline thus occurs mainly due to the contribution from  $\tilde{g}_n$  rather than  $\tilde{g}_s$ . As a consequence, the axial tension  $\tilde{l}$  is nearly constant and equal to its value at the boundary,  $\tilde{l} \approx 0$ . Figure 5 illustrates, for the case  $a/b = 10$ , that whether the term proportional to  $\tilde{l}$  is included or not in Eqs. (11), the values of  $\tilde{n}_0(-1)$  and  $\phi_c$  do not change appreciably. For this reason, in the following, we present simulation results obtained by neglecting the axial tension terms in Eqs. (11).

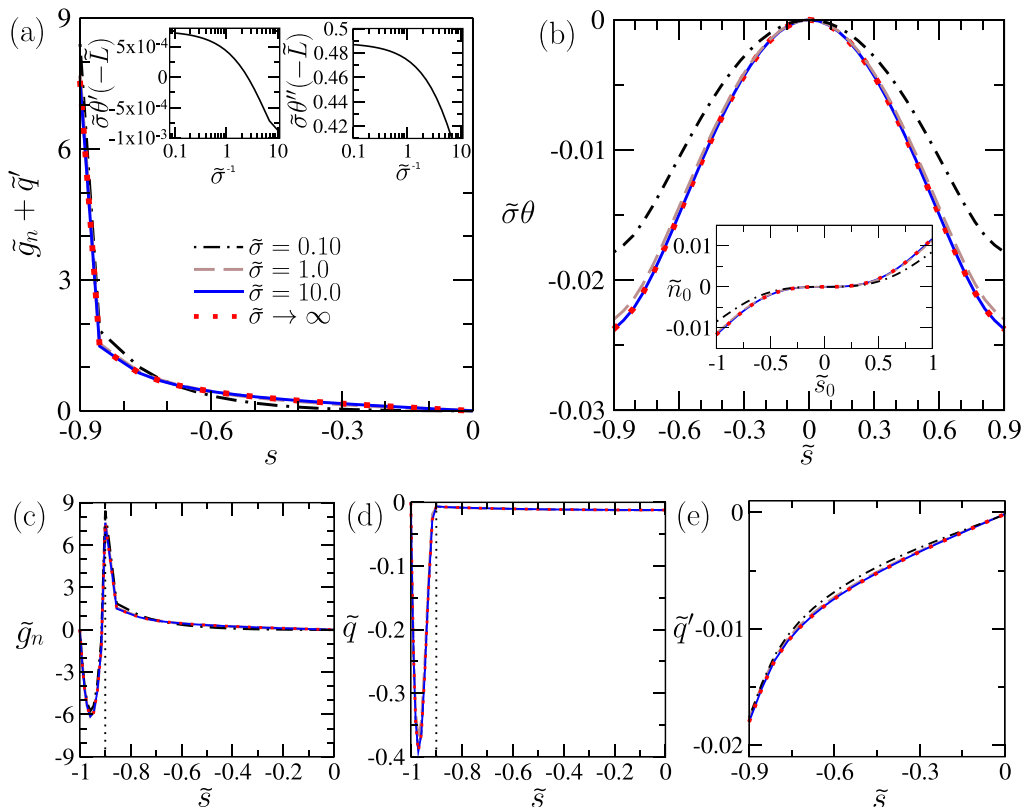


FIG. 6. Static profiles and corresponding hydrodynamic load of a platelet for different values of  $\tilde{\sigma}$ . (a) Load distribution  $\tilde{g}_n + \tilde{q}'$  in the slender region of the platelet. Inserts: Force (left) and bending moment (right) at  $-\tilde{L}$  versus  $\tilde{\sigma}^{-1}$ . (b)  $\tilde{\sigma}\theta$  versus  $\tilde{s}$ . Insert: Surface profile  $(\tilde{s}_0, \tilde{n}_0)$ . (c) Normal traction  $\tilde{g}_n$  versus  $\tilde{s}$ . The vertical dotted lines marks the location  $\tilde{s} = -\tilde{L}$ . (d) Torque density  $\tilde{q}$  versus  $\tilde{s}$ . (e)  $\tilde{q}'$  versus  $\tilde{s}$ . As in Fig. 4,  $\tilde{\lambda} = 8$  and  $a/b = 10$ .

The second observation is that, because the deflection is small, the shape of the flexible platelet can be well approximated by using the load distribution for a rigid flat platelet in Eqs. (11). To assess when this approximation is accurate, we compare profiles of  $\tilde{\sigma}\theta'''$  for finite values of  $\tilde{\sigma}$  with those for  $\tilde{\sigma} \rightarrow \infty$  [Fig. 6(a)]. A value of  $\theta$  normalized by  $\tilde{\sigma}$  is plotted in Fig. 6(b). Under this normalization, as  $\tilde{\sigma}$  increases,  $\tilde{\sigma}\theta$  collapses onto the curve corresponding to the flat platelet. The profiles of  $\tilde{\sigma}\theta'''$  and  $\tilde{\sigma}\theta$  corresponding to  $\tilde{\sigma} = 1$  and 10 are practically identical to those for  $\tilde{\sigma} \rightarrow \infty$ . For  $\tilde{\sigma} = 0.1$ , the maximum relative difference in  $\tilde{\sigma}\theta$  with respect to the rigid case is 25%. This value is still quite small, considering the relatively large flexibility of the platelet and the noticeable degree of deformation  $|\tilde{n}_0(-1)| \sim \mathcal{O}(0.1)$  associated to this stable solution compared to its undeformed shape.

### A. Effects of surface slip

We now analyze the effect of slip on the deformations of a flexible slip platelet. Because of the small deformations, we use as external hydrodynamic load the distribution corresponding to a rigid flat platelet oriented at its stable orientation angle.

Based on our analysis, the main effect of surface slip is to reduce the torque density  $\tilde{q}(\tilde{s})$  on the slender region of the platelet. This effect can be quantified by performing an asymptotic expansion of Eq. (4) for a platelet oriented at  $\phi_c$ . This analysis yields  $\tilde{q}$  to leading order in  $b/a$  about  $\tilde{s} = 0$

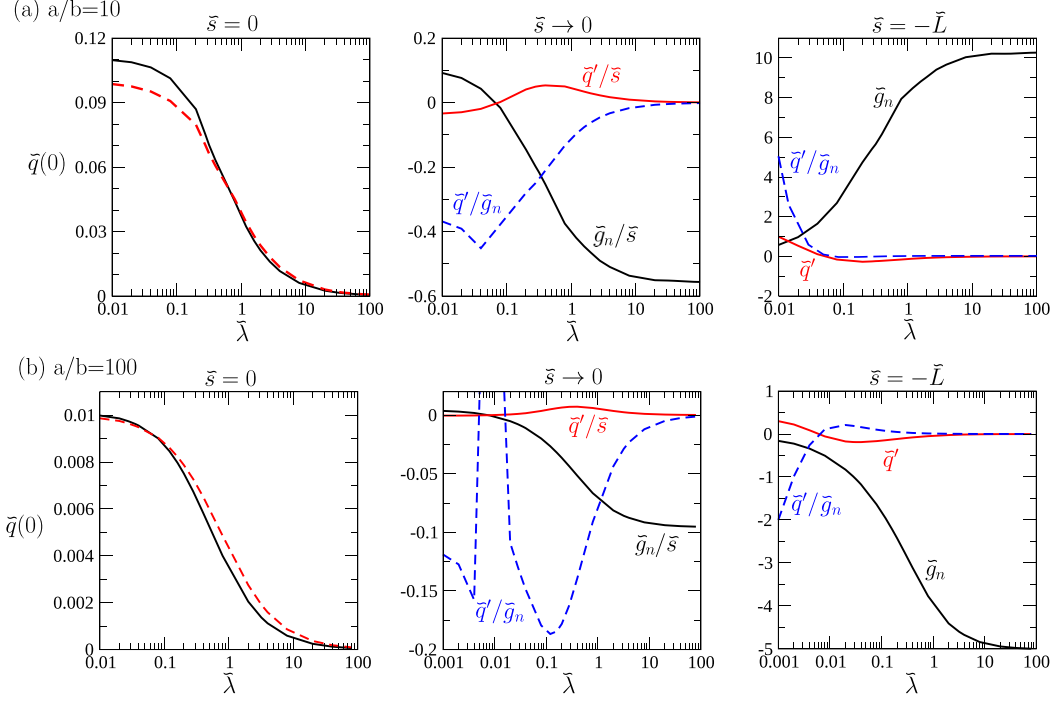


FIG. 7. Left panels: Torque density at the midpoint  $\tilde{s} = 0$  vs nondimensional slip length; black continuous lines refer to BIM simulation results, dashed red lines are analytical predictions from Eq. (15). Right panels: BIM simulations of load due to normal stresses, load due to distributed torque, and ratio of the two quantities, vs nondimensional slip length for  $\tilde{s} = -\tilde{L}$ . Central panel: normal load divided by  $\tilde{s}$ , distributed torque divided by  $\tilde{s}$ , and ratio of distributed torque to normal load, again plotted vs nondimensional slip length. The aspect ratio is (a)  $a/b = 10$  and (b)  $a/b = 100$ . In all the plots the quantities are calculated for an undeformed platelet and  $\phi = \phi_c$  (if a stable orientation exists) or  $\phi = 0$  (if a stable orientation does not exist).

[12]. The result is

$$\tilde{q}(\tilde{s}) \sim \frac{b}{a} \left[ \frac{1}{1 + c_1 \frac{\tilde{\lambda}}{(1-\tilde{s}^2)}} + \epsilon(\tilde{s}, \tilde{\lambda}) \right], \quad (15)$$

where  $\epsilon(\tilde{s}, \tilde{\lambda})$  is the additional contribution from the edges which, by symmetry, satisfies  $\epsilon(-\tilde{s}, \tilde{\lambda}) = \epsilon(\tilde{s}, \tilde{\lambda})$  and  $\epsilon(0, \tilde{\lambda}) = 0$ . The numerical prefactor  $c_1$  depends on the geometry of the platelet [12,55]. Our previous analysis shows that for a 2D platelet, i.e., a platelet of infinite depth,  $c_1 = 4/\pi$ , and that for a disk,  $c_1 = 3/2$  [12]. The condition  $\phi_c \ll 1$  is satisfied for  $a/b \gg 1$  because  $\phi_c$  decreases to zero for a given  $\tilde{\lambda}$  as  $a/b$  increases [12,33].

The leftmost panels in Fig. 7 show a comparison of  $\tilde{q}(0)$  as predicted by Eq. (15) with the simulation results. Results are plotted as a function of  $\tilde{\lambda}$  for  $a/b = 10$  (top panels) and  $a/b = 100$  (bottom panels). For  $\tilde{\lambda} \rightarrow 0$  (no-slip limit),  $\tilde{q}(0) \approx b/a$  along the surface, but as  $\tilde{\lambda} \rightarrow \infty$ ,  $\tilde{q}(0)$  vanishes because surface slip reduces the traction over the surface parallel to the shear flow. The leading order analytical solution of  $\tilde{q}(0)$  is in generally good agreement with the numerical simulations. The largest differences between the numerical and asymptotic values of  $\tilde{q}(0)$  occur for  $\tilde{\lambda} \ll 1$  and  $a/b = 10$ , which is expected by the  $O(b^2/a^2)$  error of Eq. (15).

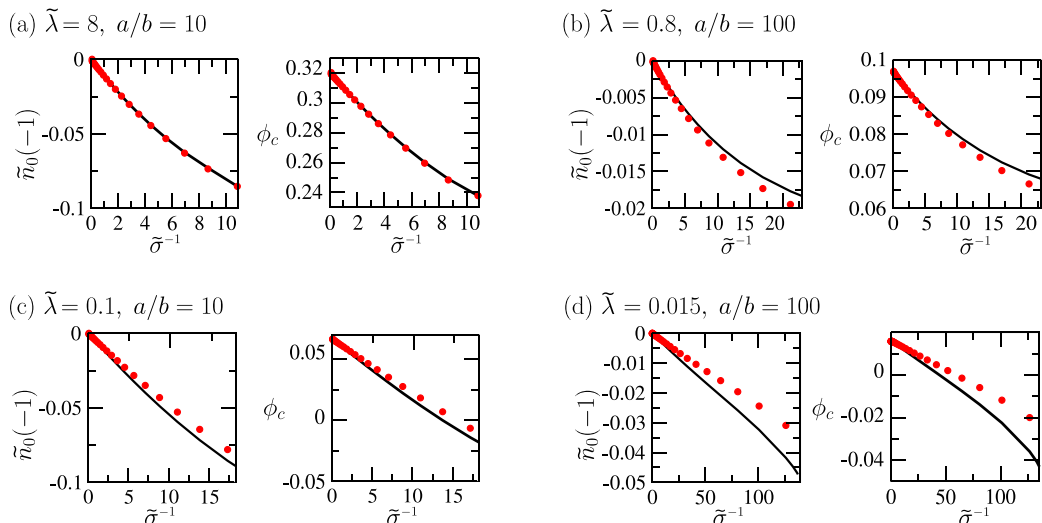


FIG. 8. Maximum deflection  $\tilde{n}_0(-1)$  and orientation angle  $\phi_c$  corresponding to the stable solution versus the inverse bending rigidity  $\tilde{\sigma}^{-1}$ , comparing simulations with the full load distribution (solid lines) with simulations with  $\tilde{q}'$  set to zero (disks). Aspect ratio and slip length values are indicated in the figure.

A similar asymptotic analysis reveals that, in the neighborhood of  $\tilde{s} = 0$ , the derivative of  $\tilde{q}$  with respect to  $\tilde{s}$  satisfies

$$\tilde{q}'(\tilde{s}) = \frac{b}{a} \cos^2 \phi_c \left[ \frac{2c_1 \tilde{\lambda} \tilde{s}}{(1 + c_1 \tilde{\lambda} - \tilde{s}^2)^2} + \epsilon'(\tilde{s}, \tilde{\lambda}) \right],$$

where  $\epsilon'(\tilde{s}, \tilde{\lambda})$  is the derivative of  $\epsilon$  with respect to  $\tilde{s}$ . Because  $\tilde{\epsilon}(0, \tilde{\lambda}) = 0$ ,  $\tilde{q}$  is independent of  $\tilde{\epsilon}$  to leading order in  $\tilde{s}$ . However,  $\tilde{\epsilon}'(0, \tilde{\lambda})$  is not zero, and therefore  $\epsilon'$  must be added in the leading order approximation. In the absence of slip, analytical solutions for  $\epsilon'$  are known for specific edge shapes [15]. In the present work we compute  $\epsilon'$  and  $\tilde{q}'$  numerically via BIM. BIM results, shown in the central and rightmost panels of Fig. 7, confirm that  $\tilde{q}'$  decreases as  $\tilde{\lambda}$  increases and vanishes asymptotically as  $\tilde{\lambda} \rightarrow \infty$ .

To understand whether  $\tilde{q}'$  contributes significantly to the load distribution and to the platelet's deformation,  $\tilde{q}'$  is compared to  $\tilde{g}_n$  for  $\tilde{s} \rightarrow 0$  and  $\tilde{s} = -\tilde{L}$  in the central and rightmost panels of Fig. 7. As expected, for  $\tilde{\lambda} \gg 1$ ,  $\tilde{q}'$  is subdominant with respect to  $\tilde{g}_n$  (the values of  $\tilde{\lambda}$  for which  $\tilde{q}' \ll \tilde{g}_n$  need not be large), suggesting that  $\tilde{q}'$  can be neglected in Eqs. (11) to leading order for  $\tilde{\lambda} \gg 1$ . However, for  $\tilde{\lambda} \ll 1$ ,  $\tilde{q}'$  is comparable or even greater than  $\tilde{g}_n$ , especially at the edges.

The fact that  $\tilde{q}'$  is comparable to  $\tilde{g}_n$ , even for relatively large values of  $a/b$ , may seem counterintuitive. Indeed, for  $\tilde{\lambda} = 0$ ,  $\tilde{q} \propto b/a$  as  $\tilde{s} \rightarrow 0$  and thus  $\tilde{q}'$  decreases as  $a/b \rightarrow \infty$ . However, asymptotic analysis of the boundary integral equation for  $b/a \ll 1$ ,  $\tilde{\lambda} = 0$  and  $\phi = 0$  reveals that  $\tilde{q}'$  and  $\tilde{g}_n$  are both proportional to  $(b/a)\tilde{s}$  for  $\tilde{s}$  near zero [15]. Our BIM simulations confirm this result: For both  $a/b = 10$  and  $a/b = 100$ ,  $\tilde{g}_n/\tilde{s}$  and  $\tilde{q}'/\tilde{s}$  are proportional to  $\mathcal{O}(b/a)$  for  $\tilde{s} \rightarrow 0$  and  $\tilde{\lambda} = 0$  (middle panels of Fig. 7), giving a ratio  $\tilde{q}'(0)/\tilde{g}_n(0)$  of 0.45 and 0.09, respectively. Hence, the distributed couple term cannot in general be neglected.

In Fig. 8, we plot the maximum deformation  $\tilde{n}_0(-1)$  and stable orientation angle  $\phi_c$  versus  $\tilde{\sigma}^{-1}$ , comparing simulations with  $\tilde{q}'$  included in Eqs. (11) with simulations in which this term is set to zero. In line with our previous analysis, we find that the effect of  $\tilde{q}'$  is more significant the smaller  $\tilde{\lambda}$ , i.e., for  $\tilde{\lambda} \gtrsim 0.1$  and  $\tilde{\lambda} \gtrsim 0.015$  for  $a/b = 10$  and 100, respectively. Further,  $\tilde{q}'$  becomes negligible for the larger values of  $\tilde{\lambda}$ , even when the deflection of the platelet becomes significantly different

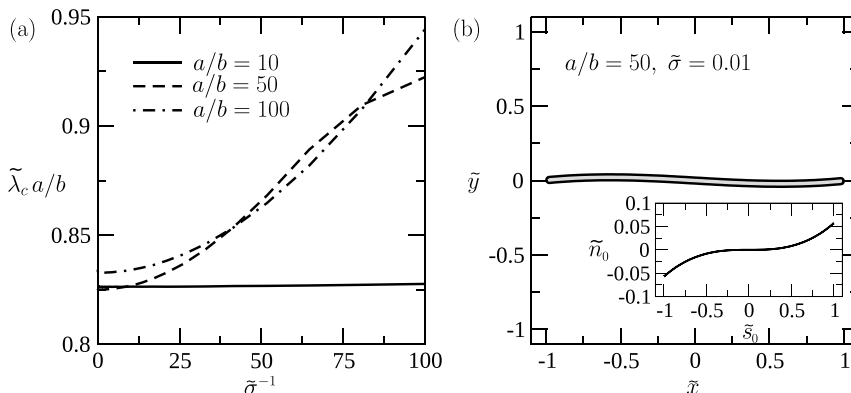


FIG. 9. (a) Critical slip length  $\tilde{\lambda}_c$  as a function of the inverse rigidity parameter  $\tilde{\sigma}^{-1}$  for  $n = 1$  and different aspect ratios. (b) Stable centerline shape for  $\tilde{\lambda} = \tilde{\lambda}_c$ ,  $\tilde{\sigma} = 0.01$  and  $a/b = 50$  in the  $(\hat{e}_x, \hat{e}_y)$  frame. Insert: Same data in the particle frame.

to an undeformed platelet, i.e., when  $\tilde{n}_0(-1) \sim \mathcal{O}(0.1)$ . For the cases where  $\tilde{q}'$  is significant, the inclusion of  $\tilde{q}'$  in the load produces larger deformations.

A stable alignment occurs when  $\tilde{\lambda} > \tilde{\lambda}_c$ . For a rigid platelet,  $\tilde{\lambda}_c$  can be calculated as the value of  $\tilde{\lambda}$  for which the total torque  $\tilde{T}(\phi = 0)$  acting on a nonrotating platelet vanishes [12]. The value  $\tilde{T}(0)$  results from a balance between the torque contributions produced by the stress over the platelet's edge and slender regions. The contributions to  $\tilde{T}(0)$  from the edge regions come mainly from the normal traction (acting on a level arm  $\sim 1$ ) and is associated to a torque vector directed in the direction opposite of the vorticity vector of the external flow field [12]. Over the slender region, the main contribution depends on the tangential traction (acting on a level arm  $\sim b/a$ ). This contribution is associated to a torque directed in the direction of the undisturbed vorticity. For no-slip, the torque contribution from the slender region is larger than the torque contributions from the edge regions, thus the platelet rotates in the direction of the vorticity vector as predicted by Jeffery [13] and by Bretherton [14]. The leading order effect of small surface slip is to decrease the torque contribution from the slender region, while the torque contributions due to the edge regions remain unchanged to leading order. Thus, there exists a critical slip length for which  $\tilde{T}(\phi = 0) = 0$ .

For a flat rigid platelet,  $\tilde{\lambda}_c a/b \approx k_n$  where  $k_n$  is a prefactor that depends on the specific shape of the platelet. For our model graphenelike platelet, the specific shape depends on the number  $n$  of layers comprising the platelet [12,33]. Correspondingly,  $k_1 \approx 0.83$  and  $k_n$  increases slightly as  $n$  is increased. We evaluate numerically how  $\tilde{\lambda}_c$  changes as a function of  $\tilde{\sigma}$ . For each  $\tilde{\sigma}$ ,  $\tilde{\lambda}_c$  is computed using a bisection method, by finding the value of  $\tilde{\lambda}$  that separates the two rotational behaviors (either the angular velocity  $\Omega \rightarrow 0$  as  $t$  increases or no stable solution exists; see Sec. III). Figure 9(a) shows  $\tilde{\lambda}_c$  as a function of  $\tilde{\sigma}^{-1}$  for different values of  $a/b$  and  $n = 1$ . The figure shows that  $\tilde{\lambda}_c$  slowly increases as  $\tilde{\sigma}$  decreases, suggesting that a flexible platelet requires a slightly larger slip length to attain a stable orientation than a rigid platelet. As  $a/b$  increases from 10 to 50,  $\tilde{\lambda}_c$  also increases. The difference in the value of  $\tilde{\lambda}_c$  for  $a/b = 100$  are less marked for  $a/b = 50$  than for  $a/b = 10$  in the given range of  $\tilde{\sigma}$ . For the smaller range of  $\tilde{\sigma}$ ,  $\tilde{\lambda}_c$  for  $a/b = 100$  is larger than for  $a/b = 50$ . This latter result suggests that a platelet with  $a/b > 100$  may require an even larger value of  $\tilde{\lambda}_c$  to align indefinitely with time in the limit  $\tilde{\sigma} \rightarrow 0$  compared with the aspect ratio range considered here.

In summary, for all the cases considered in Fig. 9(a) the effect of flexibility on  $\tilde{\lambda}_c$  is rather small. The reason for this behavior is that when the platelet is nearly aligned with the flow, which is the case when a stable orientation is achieved, the maximum deformation remains small even for relatively flexible platelets [as illustrated in Fig. 9(b) for  $\tilde{\sigma} = 0.01$ ]. As a consequence, the approximation  $\tilde{\lambda}_c a/b \approx k_n$ , developed for flat rigid platelets, holds approximately also in a range of small values of  $\tilde{\sigma}$ .

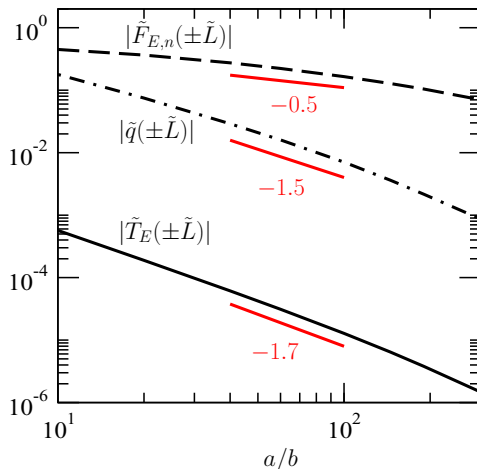


FIG. 10. Internal torque, torque density, and force at  $\tilde{s} = -\tilde{L}$  as a function of  $a/b$ . All quantities have been evaluated numerically via the BIM for a rigid undeformed platelet with  $\tilde{\lambda}a/b = 80$  and  $\phi = \phi_c$ .

### B. Effects of the edges

We first analyze effects of the edges by discussing the features of a simplified model, before considering the full load distribution. In this simplified model, the actual load distribution is replaced by the low-order polynomial given in Eq. (14). The three polynomial coefficients are obtained by fitting the boundary values  $\theta'(-\tilde{L})$  and  $\theta''(-\tilde{L})$  and the gradient of the hydrodynamic load at  $\tilde{s} = 0$  to the values corresponding to the hydrodynamic load for the rigid undeformed platelet. The fitted polynomial load and the corresponding exact solution for  $\hat{\theta}$  have already been shown in Figs. 3(a) and 3(b), respectively.

Because only one point,  $\tilde{s} = 0$ , is used to fit the polynomial to the load distribution far from the edges, the load distribution given in Fig. 3(a) does not match exactly the hydrodynamic load of Fig. 6(a), although the trends and magnitude of the computed load are respected. If the magnitude of the edge deformation, given by  $\tilde{\sigma}\theta(-\tilde{L})$ , was dependent primarily on the boundary conditions at  $\tilde{s} = -\tilde{L}$ , and not on the load distribution far from the edges, one would expect the magnitude of deflection from the simplified model to be similar to the computation with the full load. However, comparing  $\tilde{\sigma}\theta$  in Figs. 3(b) and 6(b), one sees that this is not the case: the full numerical solution gives  $\tilde{\sigma}\theta(-\tilde{L}) \approx -0.024$ , whereas the analytical solution of the simplified model predicts  $\hat{\theta}(-\tilde{L}) = \tilde{\sigma}\theta(-\tilde{L}) \approx -0.25$ . Therefore the features of the hydrodynamic load distribution far from the edges must be responsible for the small deformation obtained with the full load distribution.

Unlike the polynomial fit, the hydrodynamic load has a sudden peak as the edge region ( $\tilde{s} \rightarrow \pm\tilde{L}$ ) is approached [Fig. 6(a)]. This peak is a consequence of the edges of the platelet, and its features depend on the specific shape of the edges. Our load distribution corresponds to blunt, rounded edges. Sharp edges would give a singular, although integrable, hydrodynamic stress [56]. For slender bodies of finite thickness with orientation near  $\phi = 0$ , a boundary layer region forms in the neighborhood of  $\tilde{s} = \pm\tilde{L}$ . In this region, the traction from the slender region is matched to the traction generated in the blunt edge region [15]. The peaks seen in both Figs. 6(c) and 6(d), for respectively  $\tilde{g}_n$  and  $\tilde{q}$ , as the edge boundary is approached from the slender region are within this boundary layer region. Because the polynomial fit does not capture such a boundary layer region, the stress distribution in such region must contribute to the small deformation of the platelet.

We have seen that the sudden peak in the hydrodynamic load distribution due to the edges affects the degree of deformation of the platelet. But the actual edge forces and moments [ $\tilde{T}_E(\pm\tilde{L})$ ,  $\tilde{F}_{E,n}(\pm\tilde{L})$ , and  $\tilde{q}(\pm\tilde{L})$ ] may still also contribute to the actual degree of deformation of

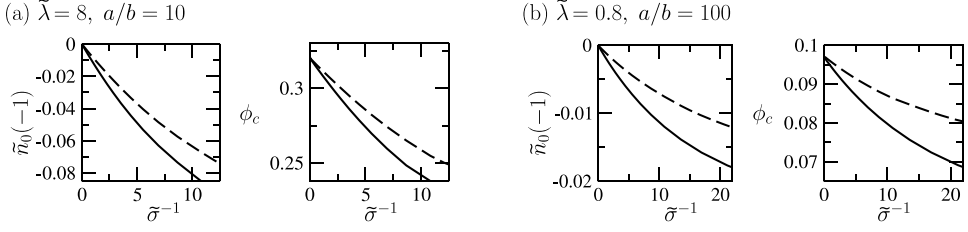


FIG. 11. Maximum deflection  $\tilde{n}_0(-1)$  and stable orientation angle  $\phi_c$  versus the inverse rigidity parameter  $\tilde{\sigma}^{-1}$ , comparing full boundary conditions (continuous line) with free-end boundary conditions (dashed line).

the platelet. In Fig. 10 we show how  $\tilde{T}_E(\pm\tilde{L})$ ,  $\tilde{F}_{E,n}(\pm\tilde{L})$ , and  $\tilde{q}(\pm\tilde{L})$  depend on  $a/b$  for a flat, rigid platelet, oriented at its stable position. As expected all quantities tend to zero as  $a/b \rightarrow \infty$ .

Because the edge moments and forces vanish as  $a/b \rightarrow \infty$ , one could assume that the free-end boundary conditions,

$$\tilde{\sigma}\theta'(\pm\tilde{L}) = 0, \quad \tilde{\sigma}\theta''(\pm\tilde{L}) = 0, \quad (16)$$

are accurate for very slender bodies. This approximation is nearly always used in the modeling of freely suspended filaments [19,43,54,57–60], sheets and ribbons [20]. To test the effect of the small but finite value of the edge load, in Fig. 11 we compare how  $\tilde{n}_0(-1)$  changes as a function of  $\tilde{\sigma}^{-1}$  for the two different boundary conditions Eqs. (10) and (16). For  $a/b = 10$  and  $a/b = 100$ , we find a difference in  $\tilde{n}_0(-1)$  of about 20% and 35% respectively depending on which boundary condition is used. For  $a/b = 10$  and  $a/b = 100$ , the free-end boundary conditions predicts a smaller value of  $\tilde{n}_0(-1)$  than the the full boundary conditions and the difference between the values of  $\tilde{n}_0(-1)$  in the two cases increases as  $\tilde{\sigma}$  decreases. Therefore, including effects of the blunt edges is necessary to achieve accurate predictions of the deformation of the platelet, at least for platelets with geometric aspect ratio up to the largest value considered here in our simulations. For even smaller  $\tilde{\sigma}$  than that examined here, such an error in the shape of the platelet could become more marked as the degree of deflection increases.

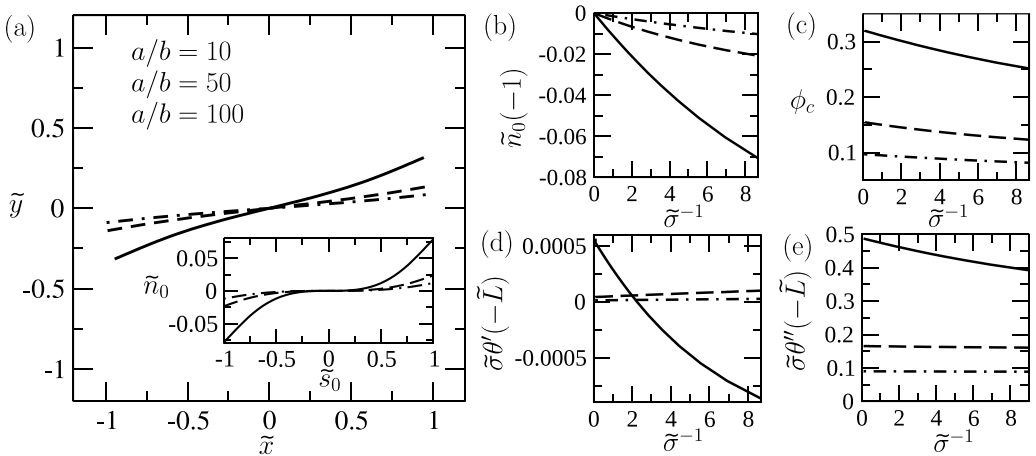


FIG. 12. (a) Centerline shapes for different aspect ratios and  $\tilde{\sigma} = 0.1$ . Insert: Stable solution of the centerline in the  $(\hat{e}_{s_0}, \hat{e}_{n_0})$  frame. The values of the slip length corresponding to the different aspect ratios are  $\tilde{\lambda} = 8$ ,  $\tilde{\lambda} = 1.6$ , and  $\tilde{\lambda} = 0.8$ . [(b) and (c)] Maximum deflection  $\tilde{n}_0(-1)$  and stable orientation angle  $\phi_c$  for the same aspect ratios as in (a). [(d) and (e)] Force and moments at  $\tilde{s} = -\tilde{L}$  for the same aspect ratios as in (a).

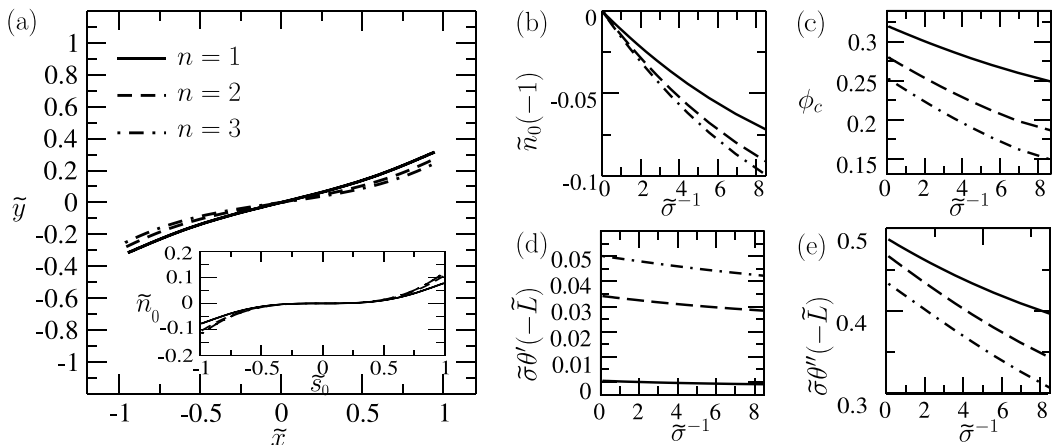


FIG. 13. Same as Fig. 12 but for varying number of stacks  $n$ . Other parameters are  $\tilde{\lambda} = 8$ ,  $a/b = 10$ , and  $\tilde{\sigma}^{-1} = 0.1$ .

To test which boundary condition affects the most the deformation of the platelet, we return to the analysis of the terms plotted in Fig. 10. In this figure,  $\tilde{F}_{E,n}(\pm\tilde{L})$  has a slower decay with  $a/b$  than  $\tilde{T}_E(\pm\tilde{L})$  or  $\tilde{q}(\pm\tilde{L})$ , suggesting that this term is the most dominant. The exponent of  $\tilde{F}_{E,n}(\pm\tilde{L})$  is comparable to that found numerically for a rectangular no-slip platelet with sharp edges in a shear flow for  $\phi = 0$  [61] and is in line with the reported exponents produced by the singular stress produced near an exterior corner [62].

A comparison of the shape of platelets for different values of  $a/b$  is shown in Fig. 12(a). Figures 12(b)–12(d) shows  $\tilde{n}_0(-\tilde{L})$ ,  $\phi_c$  and the derivatives of the solution at  $\tilde{s} = -\tilde{s}$  as a function of  $\tilde{\sigma}^{-1}$ . As seen in Figs. 12(a) and 12(b), the degree of deformation decreases as  $a/b$  increases. The value of  $\theta''(\pm\tilde{L})$  is always much greater than  $\theta'(\pm\tilde{L})$  for all values of  $a/b$ , due to  $\tilde{F}_{E,n}(\pm\tilde{L})$  being much larger than  $\tilde{T}_E(\pm\tilde{L})$ . Thus, this boundary condition, as well as the peak in the load distribution at  $\tilde{s} = -\tilde{L}$ , affects the overall deformation of the platelet more than  $\tilde{T}_E(\pm\tilde{L})$ .

As  $b$  increases for fixed  $a$ , the flat face of the edge becomes flatter. Fixing  $a/b$ , as the number of stacks  $n$  (and thus  $b$ ) increases,  $\tilde{g}_n$  also increases in the edge region, and the length of the centerline in the edge region  $|\tilde{\xi}|$  decreases. The force from the edge  $\tilde{F}_{E,n}(\pm\tilde{L})$  and the force in the boundary layer region as  $\tilde{s} \rightarrow -\tilde{L}$  will hence also change. Figure 13 compares the deformation of platelets for different values of  $n$ . As  $n$  increases  $\tilde{n}_0(-1)$  also increases, demonstrating the effect of the specific edge shape on the overall deformation of the platelet.

## V. DISCUSSION AND CONCLUSIONS

We have analysed a two-dimensional model for the deformation of a flexible platelike particle suspended in a shear flow, with a Navier-slip boundary condition applied on the particle surface. Our model is based on coupling iteratively a boundary integral equation for the fluid and an Euler-Bernoulli beam equation for the solid. The use of a boundary integral formulation that accounts for high grid refinement near the edges allows for an accurate computation of the hydrodynamic traction acting on the surface of the platelet. Such accuracy is crucial to capture the alignment and deformation of the platelet. While we have considered a specific shape of the edge relevant to 2D nanomaterials, our model should apply more generally to platelike particles and molecules.

We use our model to investigate the occurrence of stable alignments for deformable particles as a function of the nondimensional bending rigidity  $\tilde{\sigma}$  and aspect ratio  $a/b$ . Our numerical procedure allows us to find stable solutions for values of  $\tilde{\sigma}$  above a threshold rigidity parameter  $\tilde{\sigma}_c$ ; this threshold parameter is related to the specific surface of the platelet (i.e., the geometric aspect



ratio, the shape of its edges, and the value of the slip length  $\lambda$ ). As for rigid flat platelets, stable solutions are found if  $\lambda$  is approximately larger than the half-thickness of the platelet. We find that the minimum value of slip length  $\lambda_c$  that is required for the platelet to stabilize is larger for finite values of  $\tilde{\sigma}$  as compared to the rigid platelet case ( $\tilde{\sigma} \rightarrow \infty$ ). The increase in  $\lambda_c$  with decreasing  $\tilde{\sigma}$  is relatively small and depends on  $a/b$ . For example, for  $a/b = 100$  and  $\tilde{\sigma} = 0.01$ ,  $\lambda_c$  increases by about 10% compared to the case  $\tilde{\sigma} \rightarrow \infty$ . The reason to this small increase in  $\lambda_c$  is as follows. For sufficiently large slip ( $\lambda > \lambda_c$ ), the platelet is always nearly aligned with the flow. For this orientation, the compressive hydrodynamic stresses, which could lead to large-amplitude buckling, are negligible. The increase in  $\lambda_c$  is thus mostly due to a small deformation produced for  $\phi \ll 1$  by normal forces on the slender portion of the particle and localized edge effects.

A consequence of the small deflection and mild effect on  $\lambda_c$ , is that the theory of rigid slip platelets [12,33] could be used to predict the dynamics of flexible slip platelets in flow for relatively small values of  $\tilde{\sigma}$ . This is in agreement with data obtained with flexible disk-shaped aromatic molecules in shear flow using molecular dynamics simulations [32]. For these molecules, which are characterised by relatively large slip lengths, the orientational statistics were found to approximately agree with a model developed for rigid platelets.

Our model accounts for two effects that are often discarded in the modeling of elongated and flexible particles. The first effect is the inclusion of the hydrodynamic torque density, i.e., the distributed couple due to the shearing of the surfaces of the platelet by tangential hydrodynamic forces. We found that if  $\lambda \ll a$  the torque density results in an increased deflection of the platelet compared to simulations which exclude such effect.

For larger values of  $\lambda$ , the effect of the torque density becomes subdominant compared to the effect of the normal hydrodynamic load. For most platelike platelets which are not nanometric in length,  $\lambda$  is generally small. For example, for graphene,  $\lambda \approx 10$  nm and  $a$  typically 0.5–2  $\mu\text{m}$  [33]. Therefore the torque density is expected to be important in this case. The second effect is the hydrodynamic stress acting on the edges. When the platelet is nearly oriented in the flow direction, the presence of the edges is associated with a large peak in the normal hydrodynamic traction distribution. We find that the magnitude of deformation depends strongly on these peaks. Therefore, the specific structure of the edges, which affects the size of the peaks, is important even for  $a/b$  as high as 100.

An elongated particle with  $\lambda < \lambda_c$  follows some rotational orbits in a shear flow, but still spends most of its rotational period almost aligned with the flow [13]. When the particle is aligned with the flow, some of our conclusions obtained in the case  $\lambda > \lambda_c$  are expected to apply. In particular, edges are expected to be important and to have an effect on the shape of the particle. In the case of rigid elongated particles, edges are already known to have an effect on the frequency of the rotational orbits with particles with flat edges rotating faster than particles with rounded edges [15].

More broadly, our results suggest that to simulate the dynamics of particles with slip, the effect of the edges and torque density must be resolved explicitly, or at least modelled (e.g., by using local “sub-grid-scale” models, or a slender body theory approximation which accounts for the edges [63]). Fortunately, for platelike particles nearly aligned with the flow, the hydrodynamic load distribution in the case of a deformable particle is similar to that of a rigid particle. Therefore, models which calculate the deformation from a reference configuration in which the particle is not deformed could be used to develop efficient methods for deformable particles. Furthermore, our results confirm our previous observation that surface slip can arrest the rotation of platelike particles suspended in a shear flow [12], extending the theory to particles that are flexible.

#### ACKNOWLEDGMENTS

Funding from the European Research Council (ERC) under the European Union’s Horizon 2020 research and innovation programme (Grant Agreement No. 715475, project FlexNanoFlow) is gratefully acknowledged.

**APPENDIX: DERIVATION OF THE FORCE AND TORQUE BALANCE EQUATIONS**

The relationship between the generalized external hydrodynamic load, made of the tangential and normal loads plus the distributed couple, and the generalized internal force produced by the bending of the centerline can be found by solving the configuration for which  $\delta W - \delta \mathcal{E}_{\text{int}} = 0$  [64,65]. Here  $\delta W$  represents the work done by the fluid over an infinitesimal displacement  $\delta$  of  $\mathbf{x}_0$ , and  $\delta \mathcal{E}_{\text{int}}$  is the first variation of the internal energy  $\mathcal{E}_{\text{int}}$ ; for our system, the nondimensional work  $\delta \tilde{W} = \delta W / (\dot{\gamma} \eta a^3)$  is

$$\delta \tilde{W} = \int_{-\tilde{L}}^{\tilde{L}} [\tilde{\mathbf{g}}(\tilde{s}) \cdot \delta \tilde{\mathbf{x}}_0(\tilde{s}) + \tilde{q}(\tilde{s}) \delta \theta] d\tilde{s} + \tilde{T}_E(\tilde{s}) \delta \theta(\tilde{s})|_{\tilde{s}=-\tilde{L}}^{\tilde{s}=\tilde{L}} + \tilde{\mathbf{F}}_E(\tilde{s}) \cdot \delta \tilde{\mathbf{x}}_0(\tilde{s})|_{\tilde{s}=-\tilde{L}}^{\tilde{s}=\tilde{L}}, \quad (\text{A1})$$

where all length, time, and stress scales have been nondimensionlized by  $a$ ,  $1/\dot{\gamma}$ , and  $\dot{\gamma}\eta$ , respectively, and tilde is used to represent all nondimensionlized quantities. The nondimensional internal energy of a thin inextensible platelet  $\tilde{\mathcal{E}}_{\text{int}} = \mathcal{E}_{\text{int}}(\theta') / (\dot{\gamma}\eta a^3)$  is given by (see, for example, Refs. [65–68])

$$\tilde{\mathcal{E}}_{\text{int}}(\theta') = \int_{-\tilde{L}}^{\tilde{L}} \frac{\tilde{\sigma}}{2} \theta'^2 + \frac{\tilde{l}(\tilde{s})}{2} (\tilde{\mathbf{x}}' \cdot \tilde{\mathbf{x}}' - 1) d\tilde{s}, \quad (\text{A2})$$

where  $\tilde{\sigma} = \sigma_B / \dot{\gamma}\eta a^3$  is the nondimensional bending rigidity parameter and  $\tilde{l}(\tilde{s})$  is a Lagrangian multiplier, and where the prime denotes the derivative with respect to  $\tilde{s}$ . The first term on the right of the equal sign in Eq. (A2) is the energy due to bending. The second term on the right of the equal sign in Eq. (A2) is the energy due to tension, where  $\tilde{l}$  physically represents the (dimensionless) axial tension [69].

We solve  $\delta \tilde{\mathcal{E}}_{\text{int}} - \delta \tilde{W}$  for small curvature ( $\theta \ll 1$ ,  $\tilde{s}_0 \approx \tilde{s}$ ,  $\theta \approx -\tilde{h}'$ , and  $\tilde{k} \approx -\tilde{h}''$ ). Taking the first variation of  $\delta \tilde{\mathcal{E}}_{\text{int}}$ , integrating by parts where needed, and using the condition of zero total torque and force leads to

$$\begin{aligned} \delta \tilde{\mathcal{E}}_{\text{int}} - \delta \tilde{W} = & \int_{-\tilde{L}}^{\tilde{L}} [(\tilde{\sigma} \tilde{h}'''' + \tilde{l} \tilde{h}'' - \tilde{g}_n - \tilde{q}') \delta \tilde{h}(\tilde{s})] d\tilde{s} + [-\tilde{F}_{E,n}(\tilde{s}) + \tilde{q}(\tilde{s}) - \tilde{\sigma} \tilde{h}'''(\tilde{s})] \delta \tilde{h}(\tilde{s})|_{\tilde{s}=-\tilde{L}}^{\tilde{s}=\tilde{L}} \\ & + [\tilde{T}_E(\tilde{s}) + \tilde{\sigma} \tilde{h}''(\tilde{s})] \delta \tilde{h}'(\tilde{s})|_{\tilde{s}=-\tilde{L}}^{\tilde{s}=\tilde{L}} + \int_{-\tilde{L}}^{\tilde{L}} [(-\tilde{l}' - \tilde{g}_s) \delta \tilde{s}] d\tilde{s} + (\tilde{l}(\tilde{s}) - \tilde{F}_{E,s}(\tilde{s})) \delta \tilde{s}|_{\tilde{s}=-\tilde{L}}^{\tilde{s}=\tilde{L}}. \end{aligned} \quad (\text{A3})$$

Setting  $\delta \tilde{\mathcal{E}}_{\text{int}} - \delta \tilde{W} = 0$  gives

$$\tilde{\sigma} \tilde{h}'''' + \tilde{l} \tilde{h}'' - \tilde{g}_n - \tilde{q}' = 0, \quad \tilde{l}' + \tilde{g}_s = 0, \quad (\text{A4})$$

with the boundary conditions  $\tilde{\sigma} \tilde{h}''(\pm\tilde{L}) = -\tilde{T}_E(\pm\tilde{L})$ ,  $\tilde{\sigma} \tilde{h}'''(\pm\tilde{L}) = -\tilde{F}_{E,n}(\pm\tilde{L}) + \tilde{q}(\pm\tilde{L})$  and  $\tilde{l}(\pm\tilde{L}) = \tilde{F}_{E,s}(\pm\tilde{L})$ . An additional boundary condition  $\tilde{h}'(\tilde{x}_c) = 0$  [from  $\theta(0) = 0$ ] is needed to satisfy the condition of zero net torque.

For large curvature, the derivation is similar to the case  $\theta \ll 1$  presented in Eqs. (A3) and (A4) and is not repeated here (a similar derivation for large curvature is given in Ref. [64]). The equilibrium equations for large curvature are

$$\tilde{\sigma} \theta''' + \tilde{l} \theta' + \tilde{g}_n + \tilde{q}' = 0, \quad \tilde{l}' + \tilde{g}_s = 0, \quad (\text{A5})$$

with the boundary conditions

$$\begin{aligned} \tilde{\sigma} \theta'(\pm\tilde{L}) &= \tilde{T}_E(\pm\tilde{L}), \\ \tilde{\sigma} \theta''(\pm\tilde{L}) &= -\tilde{q}(\pm\tilde{L}) + \tilde{F}_{E,n}(\pm\tilde{L}), \\ \theta(\tilde{x}_c) &= 0, \\ \tilde{l}(\pm\tilde{L}) &= \tilde{F}_{E,s}(\pm\tilde{L}). \end{aligned} \quad (\text{A6})$$

In our case the central line is antisymmetric about  $\tilde{s} = 0$ , hence  $\tilde{T}_E(-\tilde{L}) = -\tilde{T}_E(\tilde{L})$ ,  $\tilde{q}(-\tilde{L}) = \tilde{q}(\tilde{L})$  and  $\tilde{F}_{E,n}(-\tilde{L}) = \tilde{F}_{E,n}(\tilde{L})$ . The boundary conditions [Eqs. (A6)] therefore simplify to

$$\begin{aligned}\tilde{\sigma}\theta'(-\tilde{L}) &= \tilde{T}_E(-\tilde{L}), \\ \tilde{\sigma}\theta''(-\tilde{L}) &= -\tilde{q}(-\tilde{L}) + \tilde{F}_{E,n}(-\tilde{L}), \\ \theta(\tilde{s}) &= \theta(-\tilde{s}), \\ \theta(0) &= 0, \\ \tilde{l}(-\tilde{L}) &= \tilde{F}_{E,s}(-\tilde{L}).\end{aligned}\tag{A7}$$

- 
- [1] Y. C. F. Soares, E. Cargnin, M. F. Naccache, and R. J. E. Andrade, Influence of oxidation degree of graphene oxide on the shear rheology of poly(ethylene glycol) suspensions, *Fluids* **5**, 41 (2021).
- [2] S. Hamze, D. Cabaleiro, and P. Estellé, Graphene-based nanofluids: A comprehensive review about rheological behavior and dynamic viscosity, *J. Mol. Liq.* **325**, 115207 (2021).
- [3] G. Zyla, A. Witek, and M. Gizowska, Rheological profile of boron nitride-ethylene glycol nanofluids, *J. Appl. Phys.* **117**, 014302 (2015).
- [4] M. S. Alqarni, R. Tabassum, M. Y. Malik, and R. Mehmood, Shape effects of molybdenum disulfide (nm) micro-rotating particles in crosswise transport of hydrogen oxide: (MoS<sub>2</sub>-H<sub>2</sub>O) nano polymer gel, *Phys. Scr.* **95**, 035002 (2020).
- [5] P. Lingard and R. Whitmore, The deformation of disc-shaped particles by a shearing fluid with application to the red blood cell, *J. Colloid Interf. Sci.* **49**, 119 (1974).
- [6] R. Nicklow, N. Wakabayashi, and H. G. Smith, Lattice dynamics of pyrolytic graphite, *Phys. Rev. B* **5**, 4951 (1972).
- [7] P. Liu and Y. W. Zhang, Temperature-dependent bending rigidity of graphene, *App. Phys. Lett.* **94**, 231912 (2009).
- [8] R. Lipowsky, The conformation of membranes, *Nature (Lond.)* **349**, 475 (1991).
- [9] R. Dimova, Recent developments in the field of bending rigidity measurements on membranes, *Adv. Colloid Interfac.* **208**, 225 (2014).
- [10] P. Poulin, R. Jalili, W. Neri, F. Nallet, T. Divoux, A. Colin, S. H. Aboutalebi, G. Wallace, and C. Zakri, Superflexibility of graphene oxide, *Proc. Natl. Acad. Sci. USA* **113**, 11088 (2016).
- [11] G. Tocci, L. Joly, and A. Michaelides, Friction of water on graphene and hexagonal boron nitride from *ab initio* methods: Very different slippage despite very similar interface structures, *Nano Lett.* **14**, 6872 (2014).
- [12] C. Kamal, S. Gravelle, and L. Botto, Hydrodynamic slip can align thin nanoplatelets in shear flow, *Nat. Commun.* **11**, 2425 (2020).
- [13] G. B. Jeffery, The motion of ellipsoidal particles immersed in a viscous fluid, *Proc. R. Soc. Lond. A* **102**, 161 (1922).
- [14] F. P. Bretherton, The motion of rigid particles in a shear flow at low Reynolds number, *J. Fluid Mech.* **14**, 284 (1962).
- [15] V. Singh, D. L. Koch, G. Subramanian, and A. D. Stroock, Rotational motion of a thin axisymmetric disk in a low Reynolds number linear flow, *Phys. Fluids* **26**, 033303 (2014).
- [16] Q. Meng and J. J. Higdon, Large scale dynamic simulation of plate-like particle suspensions. Part I: Non-Brownian simulation, *J. Rheol.* **52**, 1 (2008).
- [17] K. S. Sillmore, M. Strano, and J. W. Swan, Buckling, crumpling, and tumbling of semiflexible sheets in simple shear flow, *Soft Matter* **17**, 4707 (2021).
- [18] Y. Yu and M. D. Graham, Coil-stretch-like transition of elastic sheets in extensional flows, *Soft Matter* **17**, 543 (2021).
- [19] O. Du Roure, A. Lindner, E. N. Nazockdast, and M. J. Shelley, Dynamics of flexible fibers in viscous flows and fluids, *Annu. Rev. Fluid Mech.* **51**, 539 (2019).

- [20] T. D. Montenegro-Johnson, L. Koens, and E. Lauga, Microscale flow dynamics of ribbons and sheets, *Soft Matter* **13**, 546 (2017).
- [21] G. Batchelor, Slender-body theory for particles of arbitrary cross-section in Stokes flow, *J. Fluid Mech.* **44**, 419 (1970).
- [22] L. Koens and E. Lauga, Slender-ribbon theory, *Phys. Fluids* **28**, 013101 (2016).
- [23] R. Cortez, The method of regularized stokeslets, *SIAM J. Sci. Comput.* **23**, 1204 (2001).
- [24] Y. Xu and M. J. Green, Brownian dynamics simulations of nanosheet solutions under shear, *J. Chem. Phys.* **141**, 024905 (2014).
- [25] Y. Xu and M. J. Green, Brownian dynamics simulation of two-dimensional nanosheets under biaxial extensional flow, *J. Polym. Sci., Part B: Polym. Phys.* **53**, 1247 (2015).
- [26] C. Pozrikidis, Shear flow over cylindrical rods attached to a substrate, *J. Fluids Struct.* **26**, 393 (2010).
- [27] C. Pozrikidis, Shear flow past slender elastic rods attached to a plane, *Int. J. Solids Struct.* **48**, 137 (2011).
- [28] J. Cappello, M. Bechert, C. Duprat, O. du Roure, F. Gallaire, and A. Lindner, Transport of flexible fibers in confined microchannels, *Phys. Rev. Fluids* **4**, 034202 (2019).
- [29] S. Jogun and C. Zukoski, Rheology and microstructure of dense suspensions of plate-shaped colloidal particles, *J. Rheo.* **43**, 847 (1999).
- [30] P. Payamyar, B. T. King, H. C. Öttinger, and A. D. Schlüter, Two-dimensional polymers: Concepts and perspectives, *Chem. Commun.* **52**, 18 (2016).
- [31] J. M. Hughes, Y. Hernandez, D. Aherne, L. Doessel, K. Müllen, B. Moreton, T. W. White, C. Partridge, G. Costantini, A. Shmeliov *et al.*, High quality dispersions of hexabenzocoronene in organic solvents, *J. Am. Chem. Soc.* **134**, 12168 (2012).
- [32] S. Gravelle, C. Kamal, and L. Botto, Violations of Jeffery's theory in the dynamics of nanographene in shear flow, *Phys. Rev. Fluids* **6**, 034303 (2021).
- [33] C. Kamal, S. Gravelle, and L. Botto, Effect of hydrodynamic slip on the rotational dynamics of a thin Brownian platelet in shear flow, *J. Fluid Mech.* **919**, A1 (2021).
- [34] S. Gravelle, L. Joly, C. Ybert, and L. Bocquet, Large permeabilities of hourglass nanopores: From hydrodynamics to single file transport, *J. Chem. Phys.* **141**, 18C526 (2014).
- [35] D. Chung, Review graphite, *J. Mater. Sci.* **37**, 1475 (2002).
- [36] L. D. Landau, E. M. Lifsic, L. Pitaevskii, and A. Kosevich, *Course of Theoretical Physics: Theory of Elasticity* (Pergamon Press, London, 1986).
- [37] M. Poot and H. S. van der Zant, Nanomechanical properties of few-layer graphene membranes, *Appl. Phys. Lett.* **92**, 063111 (2008).
- [38] N. Lindahl, D. Midtvedt, J. Svensson, O. A. Nerushev, N. Lindvall, A. Isacson, and E. E. Campbell, Determination of the bending rigidity of graphene via electrostatic actuation of buckled membranes, *Nano Lett.* **12**, 3526 (2012).
- [39] H. Luo and C. Pozrikidis, Interception of two spheres with slip surfaces in linear Stokes flow, *J. Fluid Mech.* **581**, 129 (2007).
- [40] H. Luo and C. Pozrikidis, Effect of surface slip on Stokes flow past a spherical particle in infinite fluid and near a plane wall, *J. Eng. Math.* **62**, 1 (2008).
- [41] C. Pozrikidis, *Boundary Integral and Singularity Methods for Linearized Viscous Flow* (Cambridge University Press, Cambridge, UK, 1992).
- [42] S. Kim and S. J. Karrila, *Microhydrodynamics: Principles and Selected Applications* (Courier Corporation, London, 2013).
- [43] A.-K. Tornberg and M. J. Shelley, Simulating the dynamics and interactions of flexible fibers in Stokes flows, *J. Comput. Phys.* **196**, 8 (2004).
- [44] K. R. Paton, E. Varrla, C. Backes, R. J. Smith, U. Khan, A. O'Neill, C. Boland, M. Lotya, O. M. Istrate, P. King *et al.*, Scalable production of large quantities of defect-free few-layer graphene by shear exfoliation in liquids, *Nat. Mater.* **13**, 624 (2014).
- [45] Y. Y. Huang and E. M. Terentjev, Dispersion of carbon nanotubes: Mixing, sonication, stabilization, and composite properties, *Polymers* **4**, 275 (2012).
- [46] L. Landau, E. Lifshitz, A. Kosevich, and L. Pitaevskiï, *Theory of Elasticity, Vol. vii* (Butterworth, London, 1995).

- [47] N. K. Reddy, G. Natale, R. K. Prud'homme, and J. Vermant, Rheo-optical analysis of functionalized graphene suspensions, *Langmuir* **34**, 7844 (2018).
- [48] J. Eggers and M. A. Fontelos, *Singularities: Formation, Structure, and Propagation* (Cambridge University Press, Cambridge, UK, 2015).
- [49] C. Pozrikidis, *A Practical Guide to Boundary Element Methods with the Software Library BEMLIB* (CRC Press, Boca Raton, FL, 2002).
- [50] A. T. Chwang and T. Y.-T. Wu, Hydromechanics of low-Reynolds-number flow. Part 2. Singularity method for Stokes flows, *J. Fluid Mech.* **67**, 787 (1975).
- [51] J. Sherwood and G. Meeten, The use of the vane to measure the shear modulus of linear elastic solids, *J. Non-Newtonian Fluid Mech* **41**, 101 (1991).
- [52] W. H. Press, *Numerical Recipes: The Art of Scientific Computing*, 3rd ed. (Cambridge University Press, Cambridge, UK, 2007).
- [53] G. Natale, N. K. Reddy, R. K. Prud'homme, and J. Vermant, Orientation dynamics of dilute functionalized graphene suspensions in oscillatory flow, *Phys. Rev. Fluids.* **3**, 063303 (2018).
- [54] L. E. Becker and M. J. Shelley, Instability of Elastic Filaments in Shear Flow Yields First-Normal-Stress Differences, *Phys. Rev. Lett.* **87**, 198301 (2001).
- [55] S. Gravelle, C. Kamal, and L. Botto, Liquid exfoliation of multilayer graphene in sheared solvents: A molecular dynamics investigation, *J. Chem. Phys.* **152**, 104701 (2020).
- [56] D. Michael and M. O'Neill, The separation of Stokes flows, *J. Fluid Mech.* **80**, 785 (1977).
- [57] J. M. Stockie and S. I. Green, Simulating the motion of flexible pulp fibres using the immersed boundary method, *J. Comput. Phys.* **147**, 147 (1998).
- [58] S. D. Olson, S. Lim, and R. Cortez, Modeling the dynamics of an elastic rod with intrinsic curvature and twist using a regularized Stokes formulation, *J. Comput. Phys.* **238**, 169 (2013).
- [59] J. K. Wiens and J. M. Stockie, Simulating flexible fiber suspensions using a scalable immersed boundary algorithm, *Comput. Method Appl. M.* **290**, 1 (2015).
- [60] E. Nazockdast, A. Rahimian, D. Zorin, and M. Shelley, A fast platform for simulating semi-flexible fiber suspensions applied to cell mechanics, *J. Comput. Phys.* **329**, 173 (2017).
- [61] G. Salussolia, E. Barbieri, N. M. Pugno, and L. Botto, Micromechanics of liquid-phase exfoliation of a layered 2D material: A hydrodynamic peeling model, *J. Mech. Phys. Solids* **134**, 103764 (2020).
- [62] I. Mustakis and S. Kim, Microhydrodynamics of sharp corners and edges: Traction singularities, *AIChE* **44**, 1469 (1998).
- [63] R. E. Johnson, An improved slender-body theory for Stokes flow, *J. Fluid Mech.* **99**, 411 (1980).
- [64] B. Audoly and Y. Pomeau, *Elasticity and Geometry: From Hair Curls to the Non-linear Response of Shells* (Oxford University Press, Oxford, 2010).
- [65] S. K. Veerapaneni, D. Gueyffier, D. Zorin, and G. Biros, A boundary integral method for simulating the dynamics of inextensible vesicles suspended in a viscous fluid in 2D, *J. Comput. Phys.* **228**, 2334 (2009).
- [66] J. Teran, L. Fauci, and M. Shelley, Viscoelastic Fluid Response Can Increase the Speed and Efficiency of a Free Swimmer, *Phys. Rev. Lett.* **104**, 038101 (2010).
- [67] Ou-Yang Zhong-can and W. Helfrich, Bending energy of vesicle membranes: General expressions for the first, second, and third variation of the shape energy and applications to spheres and cylinders, *Phys. Rev. A* **39**, 5280 (1989).
- [68] M. Abbasi, A. Farutin, H. Ez-Zahraouy, A. Benyoussef, and C. Misbah, Erythrocyte-erythrocyte aggregation dynamics under shear flow, *Phys. Rev. Fluids* **6**, 023602 (2021).
- [69] E. Hinch, The distortion of a flexible inextensible thread in a shearing flow, *J. Fluid Mech.* **74**, 317 (1976).